In Situ Intermediates Determination and Cytotoxicological Assessment in Catalytic Oxidation of Formaldehyde: Implications for Catalyst Design and Selectivity Enhancement under Ambient Conditions

Haiwei Li,[†] Long Cui,[†,‡] Yanfeng Lu,[‡] Yu Huang,[‡] Junji Cao,[‡] Duckshin Park,[§] Shun-cheng Lee,*[,†] Wingkei Ho*[,∥]

[†]Department of Civil and Environmental Engineering, The Hong Kong Polytechnic University, Hong Kong, China.

[‡]State Key Laboratory of Loess and Quaternary Geology (SKLLQG) and Key Laboratory of Aerosol Chemistry and Physics, Institute of Earth Environment, Chinese Academy of Sciences, Xi'an 710061, China.

[§]Transportation Environmental Research Team, The Korea Railroad Research Institute, Gyeonggi-do, South Korea.

[∥]Department of Science and Environmental Studies and State Key Laboratory in Marine Pollution, The Education University of Hong Kong, Hong Kong, China.

Correspondence and requests for materials should be addressed to Prof. Shun-cheng Lee (Email: ceslee@polyu.edu.hk) or to Dr. Wingkei Ho (Email: keithho@eduhk.hk).

ABSTRACT: Formation and decay of formaldehyde oxides (CH_2OO) impact the complete oxidation of formaldehyde. However, speciation and reactivity of CH_2OO are poorly understood because of its extremely fast kinetics and indirect measurements. Herein, three isomers of CH_2OO (i.e., main formic acid, small dioxirane, and minor CH_2OO Criegee) were *in situ* determined and confirmed as primary intermediates of the room-temperature catalytic oxidation (RCO) of formaldehyde with two reference catalysts, i.e., $TiO_2/MnO_x–CeO_2$ and $Pt/MnO_x–CeO_2$, respectively. CH_2OO Criegee is quite reactive, whereas formic acid and dioxirane have a longer lifetime. The production, stabilization, and removal of the three intermediates are preferentially at higher humidity, matching well with the decay rate of CH_2OO at approximately 6.6×10^3 s^{-1} in humid feed gas faster than 4.0×10^3 s^{-1} in dry feed. By contrast, given that a thinner water/TiO_2 interface was well-defined at $TiO_2/MnO_x–CeO_2$, fewer reductions in the active sites and catalytic activity were found when the humidity was decreased. Furthermore, lethal intermediates more captured at the $TiO_2/MnO_x–CeO_2$ surface suppressed the toxic off-gas emissions. This study provides practical insights into the rational design and selectivity enhancement of reliable catalytic process for indoor air purification under unfavorable ambient conditions.

INTRODUCTION

Formaldehyde oxides (CH_2OO), the simplest carbonyl oxides or Criegee intermediate, have been recognized as important transient intermediates in tropospheric oxidation[1-5] but have been rarely studied in catalytic oxidation of formaldehyde (CH_2O). A large fraction of CH_2OO in the atmosphere, whose longest lifespan is observed in 0.05–2 ms[2, 6], incurs extremely reactive bimolecular reactions with species such as trace gases (e.g., SO_2 and NO)[2], peroxy radical and organic acid[3, 4, 7], and water vapor[5]. Only a few reports[2, 4, 5] on direct measurements of CH_2OO are available. CH_2OO Criegee and its isomers (i.e., formic acid and dioxirane)[6, 8] are identified through vacuum ultraviolet photoionization mass spectrometry in a chamber simulation of CH_2I_2/O_2 photolysis[2, 4]. The decay rate of CH_2OO reaction with water vapor at high relative humidity (RH = 85%) is much faster than that with CH_2OO scavengers, such as SO_2 and NO_2 in a relatively dry atmosphere (RH = 35%)[5, 9].

Is the CH_2OO chemistry similar in catalytic oxidation of CH_2O? Room-temperature catalytic oxidation (RCO) using either transition metal-based catalysts or noble metal-based catalysts has become an energetically attractive approach to reduce CH_2O in indoor air[10-13]. As diurnal or regional variations in ambient temperature and humidity, RCO of CH_2O has been subjected to the limits in the moisture-dependent activity at low temperatures[14-16]. Our group has thus focused on the surface hydrophilic modification of the RCO catalysts. With the capability of active-site exposure and activation of reactive oxygen species at low temperatures, MnO_x–CeO_2 catalyst (MCO) is often modified by other catalysts or elements in hybrid fabrications[17-19]. Accordingly, MCO supported colloidal TiO_2 catalyst[20] was synthesized to form a water/TiO_2 interface[21-23], resulting in approximately 41% (dry air) of the recycling activity comparable with 57% in high humidity at room temperature. To date, making direct measurements of CH_2OO

intermediates in the oxidation of CH_2O is challenging, they are roughly estimated by the proposed bridging modes of carboxylic groups[14, 15, 24]. Two primary CH_2OO intermediates, i.e., formic acid (10.82 eV) and dioxirane (11.33 eV), were preliminarily identified at different photoionization energies by *in situ* time-of-flight photoionization mass spectrometry. The formation of the two intermediates favors moistures as supported by evidence of the hydroxymethyl hydroperoxide ($HOCH_2OOH$, HMHP) yield from the reaction of CH_2OO with water vapor[2, 20, 25]. These findings help elucidate the complete reaction pathway of CH_2O oxidation. Nevertheless, the production, stabilization, and removal of CH_2OO have been not fully studied. Additionally, potential environmental impacts from the released CH_2OO intermediates remain unknown, although the toxicity of formaldehyde is well reported[26-28].

Herein, *in situ* determinations of the CH_2OO speciation and kinetics during the RCO of CH_2O were investigated through vacuum-ultraviolet time-of-flight photoionization mass spectrometry. The RCO of CH_2O was examined over two different MnO_x–CeO_2-based catalysts, namely, MnO_x–CeO_2 supported TiO_2 and MnO_x–CeO_2 supported Pt (denoted as TO/MCO and Pt/MCO, respectively). Here the TO/MCO and Pt/MCO catalysts were modified and characterized after the loading treatment was administered to attain an interfacial hydration structure[20, 21, 29, 30]. In comparisons with Pt/MCO, a thinner ordered interface between molecular water and rutile TiO_2 surface was explored at TO/MCO. As such, their adsorption and complete oxidation of CH_2O to CO_2 were compared in humid and dry feeds. A cytotoxicological study of the spent catalysts after the reaction was terminated towards yeast cells was conducted to further evaluate the inhibition of toxic intermediate emissions as compared to the cytotoxicity of the fresh catalysts and formaldehyde.

MATERIALS AND METHODS

Catalyst Synthesis. The preparations of the precursor MCO and TO/MCO are described in **Supporting Information (SI)**. Pt/MCO was prepared via a wet impregnation route. In brief, a total of 500 mg of the as-prepared MCO was added dropwise to a mixture of 30 mL of ultrapure water (Milli-Q system, Millipore Inc.) and 5 mL of H_2PtCl_6 (2 mg·mL^{-1}) aqueous solution under stirring. After impregnation for 30 min, 10 mL of the mixed solution of $NaBH_4$ (0.1 mol·L^{-1}) and NaOH (0.5 mol·L^{-1}) was rapidly injected into the suspension until to uniformly contact with the whole surface of the suspension under stirring. The molar ratio of Pt : $NaBH_4$: NaOH approximated to 1 : 5 : 25. After reduction for 30 min, the final suspension was washed and centrifugated with ultrapure water five times and dried in an oven at 65 °C for 6 h. The mass ratio of Pt to MCO was determined to be 1.8% (**SI Table S1**).

Characterizations. Powder X-ray diffraction (XRD) of the as-prepared catalysts was performed using Philips X'pert Pro Super diffractometer with Cu Kα radiation (λ = 0.15406 nm). The high-resolution micromorphology was observed under a JEOL JEM-2010 transmission electron microscope (TEM). The Brunauer-Emmett-Teller (BET) surface area was obtained by N_2 adsorption/desorption isotherms at 77 K on a Micrometrics Gemini VII 2390 instrument. Elemental contents were precisely determined by inductively coupled plasma-atomic emission spectroscopy on a Vista MPX ICP system (Varian). X-ray photoemission spectroscopy (XPS) was performed on a Thermo ESCALAB 250 system, and all of the binding energies were calibrated to the C 1s peak at 284.8 eV of the surface adventitious carbon. Pyridine adsorbed IR spectroscopy (Py-IR) was conducted with Fourier transform infrared (FT-IR; Tensor 27, Bruker, Germany) spectroscopy equipped with an *in situ* vacuum (10^{-3} Pa) IR cell reactor. The sample was purged with pure He gas at a heating rate of 10 °C·min^{-1} to 400 °C and then cooled to room temperature in the vacuum cell. Pyridine vapor was *in situ* introduced until the adsorbed pyridine

approached saturation. The desorption of the adsorbed sample was conducted at a similar heating rate of 10 °C·min^{-1} to 450 °C. The Py-IR spectra were obtained with a resolution of 4 cm^{-1} (32 scans). The OH stretching region (2800–3800 cm^{-1}) at the surface of catalysts was characterized by sum frequency generation (SFG) spectroscopy (**SI Figure S1**).

***In Situ* C 1s XPS Analysis.** *In situ* XPS studies were investigated using a Vacuum Generators Escalab 220 XL spectrometer equipped with monochromatized aluminum X-ray irradiation (Al Kα = 1486.6 eV) and an *in situ* cell reactor. The CH_2O-saturated sample was preheated from 25 °C to 175 °C under an Ar feed gas at a rate of 2 °C·min^{-1}. The sample was cooled under the Ar feed gas to 25 °C after the required temperature was reached, and *in situ* XPS analysis was performed in the cell reactor. The C 1s XP spectra were fitted by a peak-fitting program with a mixed Gaussian (70%)/Lorentzian (30%) peak shape.

Catalytic Activity Test. Catalytic oxidation of CH_2O was conducted in a thermostatic fixed-bed reaction system. Gaseous CH_2O was diluted with a carrier gas (5 ppm CH_2O/21% O_2/N_2 balance, RH = 0.7%–90%, GHSV = 6 × 10^4 h^{-1}), and 0.15 L·min^{-1} of the gas flow rate and 5 ppm of inlet CH_2O concentrations were stoichiometrically determined by a mass flow controller (Brooks 5860E). Afterwards, 50 mg of test catalysts sieved between 40 and 60 mesh was loaded on silica wool in a stainless-steel thermocouple tube (8 mm diameter) of the fixed-bed reactor. The relative humidity during the reaction was controlled by adjusting the ratio of humid air in the carrier gas and temperature was controlled with T-measuring thermocouples inside the stainless-steel tube. The outlet concentrations of CH_2O and CO_2 were monitored with a photoacoustic multi-gas monitor (Model 1412i, LumaSense INNOVA Technologies Inc., Denmark). The error bars (standard deviation) in the activity tests were calculated from repeat measurements.

***In Situ* Measurements of CH_2OO.** CH_2OO speciation and kinetics were directly determined through vacuum-ultraviolet time-of-flight photoionization mass spectrometry. A schematic of the experimental setup is given in **SI Figure S2.**

Confocal Microscopy of Spent Nanoparticles towards Yeast Cells. Yeast (*Saccharomyces cerevisiae*, JCM 7255) was incubated with agitation at 30 °C in a YE medium (5.0 $g \cdot L^{-1}$ yeast extract and 30 $g \cdot L^{-1}$ glucose). After the yeast suspension was centrifugated at 8000 ×g at 3 °C for 10 min, the harvested yeast cells in the late exponential growth phase were washed thrice with the sterilized NaCl aqueous solution (5 mM). NaCl aqueous solution was also used as the dispersion medium.

The nanoparticles (NPs) were subjected to toxicity tests. Prior to cell exposure, the spent NPs were sealed instantly in storage at 3 °C when the CH_2O-exposed reaction was terminated. The yeast suspension with initial concentrations of 1×10^6 $cells \cdot mL^{-1}$ was exposed to the NP suspension with different concentrations of 0.5, 5, 10, 25, 50, and 100 $\mu g \cdot mL^{-1}$ in 5 mM aqueous NaCl solutions in a sterilized microtube. Next, the microtube was moved on a Duck rotor at 60 rpm for 1 h at 30 °C. The mixture suspension was spread on YE agar plates for 1-h incubation at 30 °C. The cell suspension without NPs on a YE agar (2.0% [w/v]) plate was tested as a control group. Toxicity was evaluated with the colony-forming units (CFUs) counting of living cells given in the fluorescence imaging by fluorescence cellular scanning microscopy (FCSM) with a 488 nm laser for excitation (Olympus laser-based point scanning FV-1000D confocal fluorescent microscope). The viability of the cells was discriminated by staining the combination of two membrane-permeable dyes, namely, propidium iodide (PI) and 4′,6-diamidino-2-phenylindole (DAPI). PI only infiltrates cells with a disrupted membrane, and DAPI can enter all cells. Live cells were labeled with a green fluorophore in the fluorescence images, while disrupted or dead

cells were marked with a purple fluorophore.

RESULTS AND DISCUSSION

Assembly of Hydrophilic Interface Favorable to Active-site Exposure. Exploring a water/metal oxide interface of RCO catalysts is crucial to their practical applications in the CH_2O removal at unfavorable reaction temperatures and moistures. Aside from the enlarged specific surface area and pore volume (**SI Table S1**), the surface modifications with TiO_2 and Pt loading, which exhibit an ordered array of the hydrophilic interfacial structure at the vicinity of their surfaces[15, 20, 21, 29, 30], are examined to improve the adsorption and catalytic oxidation of CH_2O. First, the crystal structure and morphology of TO/MCO and Pt/MCO are illustrated in **Figures S3 and S4 of SI**, respectively. TO/MCO shows approximately 5 nm thin loading of TiO_2 with a uniformly exposed anatase facet (101) on the MCO surface, while a small size (approximately 2.4 nm) distribution of Pt nanoparticles for Pt/MCO retains the unchanged morphology, particle size, and exposed facets of the precursor MCO.

The structural arrangement of water molecules at TO/MCO and Pt/MCO was characterized through sum frequency generation (SFG) spectroscopy[29, 31] in an internal reflection mode as a function of the energy of infrared radiation (IR). The SFG spectra in the hydroxyl molecules (OH) stretching vibration region were generally featured by two broad peaks approximately at *ca.* 3200 and 3400 cm^{-1}. They are assigned to the symmetric OH stretching of water molecules (i.e., strongly hydrogen bonded "ice-like" water structure) and the asymmetric OH stretching in a more random arrangement (i.e., less ordered ''liquid-like'' water), respectively[31]. In **Figures 1a–b**, two broad peaks for Pt/MCO were observed in the OH stretching region (2800–3800 cm^{-1}) at *ca.* 3200 and 3450 cm^{-1}. By contrast, two broad OH bands for TO/MCO were centered at *ca.* 3200 cm^{-1} and a slightly low wavenumber at *ca.* 3400 cm^{-1}. The SFG spectra prove that the

highly-ordered “ice-like” interfacial water molecules were distributed at the vicinity of the clean surface of TO/MCO and Pt/MCO, based on the IR study of water clusters. The potential dependence of interfacial water at TO/MCO and Pt/MCO was also investigated. The SFG spectra of OH bands, which were fitted as the equation of SFG intensity (**SI Equation S1**), can be considered as an index of the order of the interfacial water and varied as surface oxide is formed. The SFG intensity weakened after the maximum was reached at zero potential in the Pt/MCO electrode when the potential changes from positive (200 mV) to negative (–400 mV). Conversely, the intensity sharply increased as the potential in the TO/MCO electrode was decreased. The charge of the TO/MCO surface was higher than that of Pt/MCO (**SI Figure S5**). Accordingly, oxygen-up and oxygen-down orientations were stimulated on negatively and positively charged surfaces, respectively. Consequently, the ordered water layer at the vicinity of the TO/MCO surface became thin. CH_2O adsorption, which is initiated by the hydroxyl bonding of water molecules preferable with the methyl groups of formaldehyde and formate intermediates[32], is feasible at this interfacial hydrophilic structure even in a dry atmosphere.

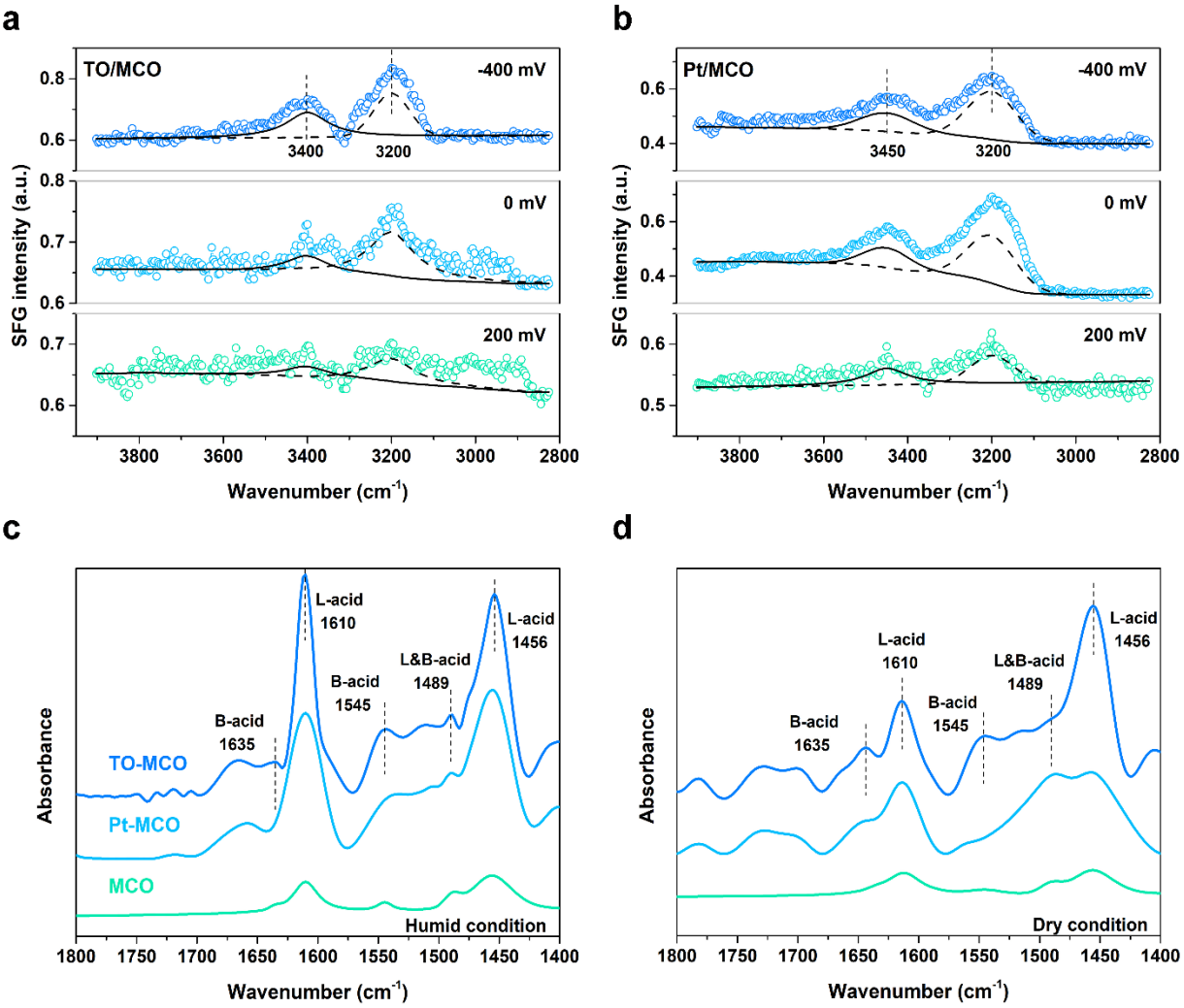

187

188 **Figure 1.** Potential dependence of the SFG spectra in the OH stretching region (2800–3800
189 cm^{-1}) at the surface of TO/MCO (a) and Pt/MCO (b) electrodes in a 0.1 M $HClO_4$ electrolyte
190 solution. SFG spectra were fitted by two broad OH bands centered at low (dash line) and high
191 (solid line) wavenumbers. Py-IR measurements of active sites over TO/MCO and Pt/MCO under
192 humid (c) and dry (d) conditions, respectively.

193 Next, the effects of moisture on surface active-site behaviors were investigated through
194 pyridine-IR (Py-IR) measurements[33]. Two kinds of surface metal sites, namely, Lewis acid (L-
195 acid) and Brønsted acid (B-acid) sites, are discussed due to free electron and proton exchange at
196 metallic catalysts. The Lewis acid–base properties of the metal oxides, ascribed to the cyclic

electron transfer, have important implications for the oxidation selectivity and activation of reactive oxygen of catalysts.[20, 34-36] In **Figures 1c–d**, the peaks at approximately *ca.* 1456 and 1610 cm^{-1} bands were related to pyridine adsorbed onto L-acid sites, and the peaks at approximately *ca.* 1545 and 1635 cm^{-1} bands were assigned to B-acid sites. The peak at *ca.* 1489 cm^{-1} originated from pyridine adsorbed onto L-acid and B-acid sites, and the peak at *ca.*1474 cm^{-1} was assigned to the C–H exchange or hopping of hydrocarbon compounds to oxygen atoms[33, 34]. In comparison with Pt/MCO under humid conditions, TO/MCO shows a high degree of nucleophilic substitution (an exchange of metal sites (M) with oxygen atoms (O), namely the formation of M–O structure), where the Brønsted/Lewis (B/L) ratio at TO/MCO was 0.51 lower than that at Pt/MCO with 0.64. In the dry feed, TO/MCO maintained sufficient exposure of the L-acid site with a B/L ratio of 0.67, whereas an apparent decrease in L-acid sites was found at Pt/MCO with 0.80. L-acid sites are restricted if ion exchanges appear between metal ions and protons[33], and Brønsted acid sites become to act as predominant active sites at high temperatures (>200 °C)[34, 37]. Molecular water at the vicinity of metal oxides induces a proton transfer to form a water dimer with the hydroxyl overlayer[21, 33], which comprises $H_5O_2^+$. More L-acid sites were found at TO/MCO in humid air possible because of formation of the water dimer. Hence, the effect of a water dimer on the as-generated porous water layer of TO/MCO is substantial, leading the L-acid sites to become predominant. These events can facilitate the activation of surface oxygen species into reactive oxygen species, which was induced by cyclic electron transfer at the active sites in metallic dismutation reactions[20].

High-resolution XPS spectra (**SI Figure S6**) were obtained to study the ion exchange at TO/MCO and Pt/MCO before and after the reaction and to further verify the effects of moisture on the active-site behaviors. High oxidation states (Mn^{4+}) were maintained (see also **SI Figure**

220 **S7**). After the reaction was terminated, the increased proportions of surface Mn^{4+}/Mn^{3+} ranged
221 from 2.73 to 3.27 at TO/MCO. A few losses of surface oxygen species occurred at TO/MCO
222 throughout the dismutation reactions, in which the ratios of surface lattice oxygen (O_{latt}) to
223 surface adsorbed oxygen (O_{ads}) remained at 0.34–0.36. Ti–O depositions on O-defect sites of
224 MnO_x–CeO_2[20, 38, 39] remediated the participation of oxygen species in TO/MCO (see also more
225 intense O 1s XPS signal in **SI Figure S3b**). Selective electron transfers from Ce^{4+} to Mn^{3+}
226 enhanced the charge storage of the neighboring MnO_x in the bimetallic (Mn–Ce) dismutation
227 system[20]. Hence, a few Ce^{4+} reactions with proton ions decreased L-acid sites. By contrast, the
228 XPS spectra show distinct changes in O 1s, Mn 2p, and Pt 4f peaks in Pt/MCO during the
229 reaction. O_{latt}/O_{ads} ratio increased from 0.17 to 0.28, whereas large reductions in Mn^{4+}/Mn^{3+} were
230 found from 3.41 to 1.69. The coexistence of the metallic and oxidized Pt was observed. The
231 oxidation states of Pt were increased throughout the reaction, where free electrons could be
232 released to support the potential-dependent hydration structure and the electron-dependent Lewis
233 active sites of Pt/MCO shown in Figure 1. In comparison with TO/MCO and MCO, the binding
234 energies (BE) of O_{latt}, O_{ads}, and Mn $2p_{3/2}$ peaks shifted to low values in Pt/MCO, indicating a
235 strong charge exchange in metal-support interactions[40, 41]. These findings demonstrate that
236 accepting negative charges[41] on Mn and O sites from the oxidized Pt can facilitate the activation
237 of reactive oxygen species[42]. However, the generation of more Mn^{3+} in Pt/MCO was verified by
238 the low BE shift of Mn. Consequently, failure to maintain a high oxidation state of metal oxides
239 affects the interfacial water structure and the M–O bridging mode.

240 Overall, L-acid sites play a key role in the selectivity for the cleavage of carbonyl and
241 carboxylic species[20, 33, 34]. The active-site exposure and oxidation selectivity of the RCO catalysts
242 under unfavorable reaction conditions can be controlled by precisely adjusting the molar ratio of

metallic ions.

***In Situ* Measurements of CH_2OO Speciation and Kinetics.** Direct measurements of CH_2OO species were performed using by the time-of-flight photoionization mass spectrometry in **Figure 2**. The millisecond's resolution of the mass spectrometer is sufficient to determine the photoion signal of the CH_2OO group (mass/charge (*m/z*) =46 peak) arisen from the catalytic oxidation of CH_2O. First, the time-of-flight photoion signal of CH_2OO was carefully calibrated following the reported photoionization mass spectrometric detection of CH_2OO[2], which was formed in the $CH_2I + O_2$ reaction after the 248 nm photolysis of CH_2I_2/O_2 (**SI Figure S8**). The kinetic profile of the CH_2OO in the CH_2I_2/O_2 system followed the pseudo-first-order kinetics scheme as the decay rate of CH_2OO was fitted constant. The formation and removal of CH_2OO were well proportionate with those of precursor CH_2I. The decay of CH_2OO was independent of O_2 concentrations, suggesting that CH_2OO can be directly measured under ambient conditions. Here the CH_2OO lifetime was correlated with the decay of CH_2O (*m/z* = 30) over catalysts (see **Figure 2a**) and calibrated from C_2H_6O via time-of-flight distribution of the *m/z* = 46 signal (see **Figure 2b**). Very faint photoionization signal at *m/z* = 64 was assigned to hydroxymethyl hydroperoxide ($HOCH_2OOH$, HMHP). The kinetic analysis of HMHP chemistry remains uncertain and is thought to be generated from the reaction of CH_2OO with water molecules[2, 8].

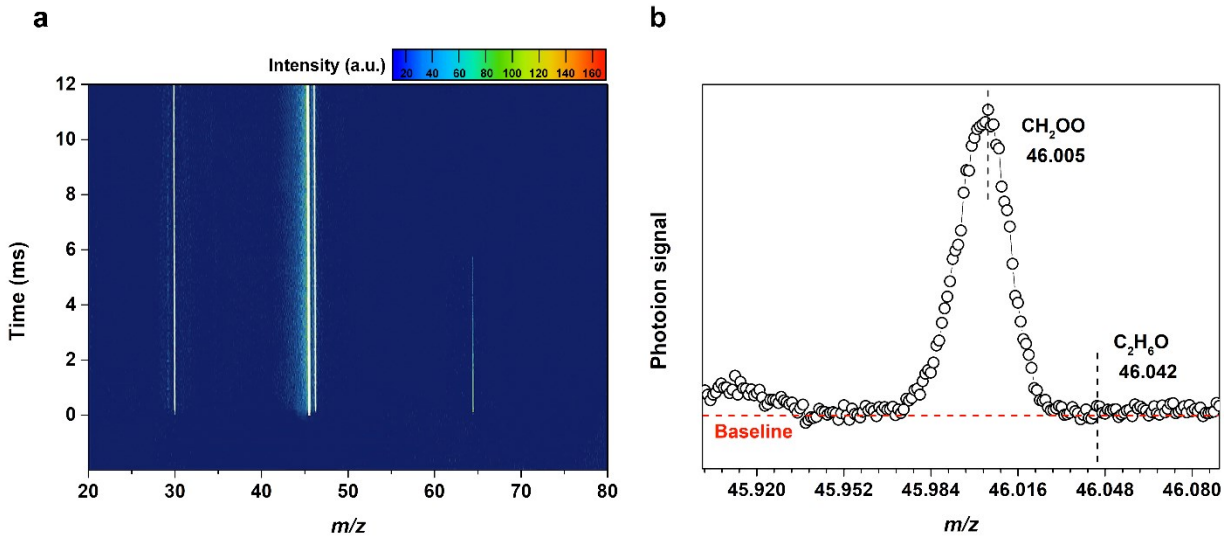

Figure 2. Time-resolved photoionization mass spectra of CH_2OO signal during the catalytic oxidation of CH_2O (a). Time-of-flight distribution of the m/z = 46 photoion signal (b).

In **Figure 3**, the photoionization spectra of the CH_2OO isomers were identified by scanning the ionizing photon energy, and impacts from moistures on the photoionization intensity of the isomers were studied in the reaction of CH_2O with TO/MCO and Pt/MCO. The signal integration of CH_2OO photoionization spectrum is roughly the integral sum of photoion signal of the three isomeric coproducts with different photoionization energies, which were also calibrated in the CH_2I_2 ozonolysis system (**SI Figure S9**). Dioxirane and formic acid were identified in much higher ionization energies at 10.83 eV and 11.31 eV, respectively. The spectrum originated from only 0.05 eV was assigned to CH_2OO Criegee, which is much smaller than the theoretical predictions of 9.98 eV[43]. CH_2OO Criegee is thought to possess some single bond characters[2, 6, 25, 43], which are ascribed to a rapid dissociation of C–C and O–O bonds from the ozonolysis of unsaturated hydrocarbons. This work cannot completely rule out CH_2OO Criegee because it is probably involved in side or secondary processes (e.g., HMHP production from CH_2OO reaction with H_2O or CH_2O regeneration)[2, 25]. The CH_2OO formations were comparable between

TO/MCO and Pt/MCO at a higher RH of 72% but turned to diminish over Pt/MCO much larger than that over TO/MCO with the lowering moistures. These observations are well consistent with higher CH_2O removal efficiencies of TO/MCO than Pt/MCO in various humid levels (see **Figures 5c**–**d**). The photoion signals of formic acid that remained the highest in various humid levels indicate the main primary intermediate. Formations of the small dioxirane and minor CH_2OO Criegee intermediate are estimated through further thermal isomerization or dissociation from carboxylic groups (the symmetric υ_s and asymmetric stretching υ_{as} [COO])[2, 5]. These results match the recently reported *in situ* FT-IR study, wherein the formations of δ [CH_2] corresponding to υ_s [OH] are correlated with the decay of υ_s [CH] groups[20]. Hence, compared with minor formic acid and dioxirane observed in the atmospheric oxidation[2, 5, 8], main formic acid and dioxirane account for a substantial proportion in the CH_2OO group in the oxidation of CH_2O.

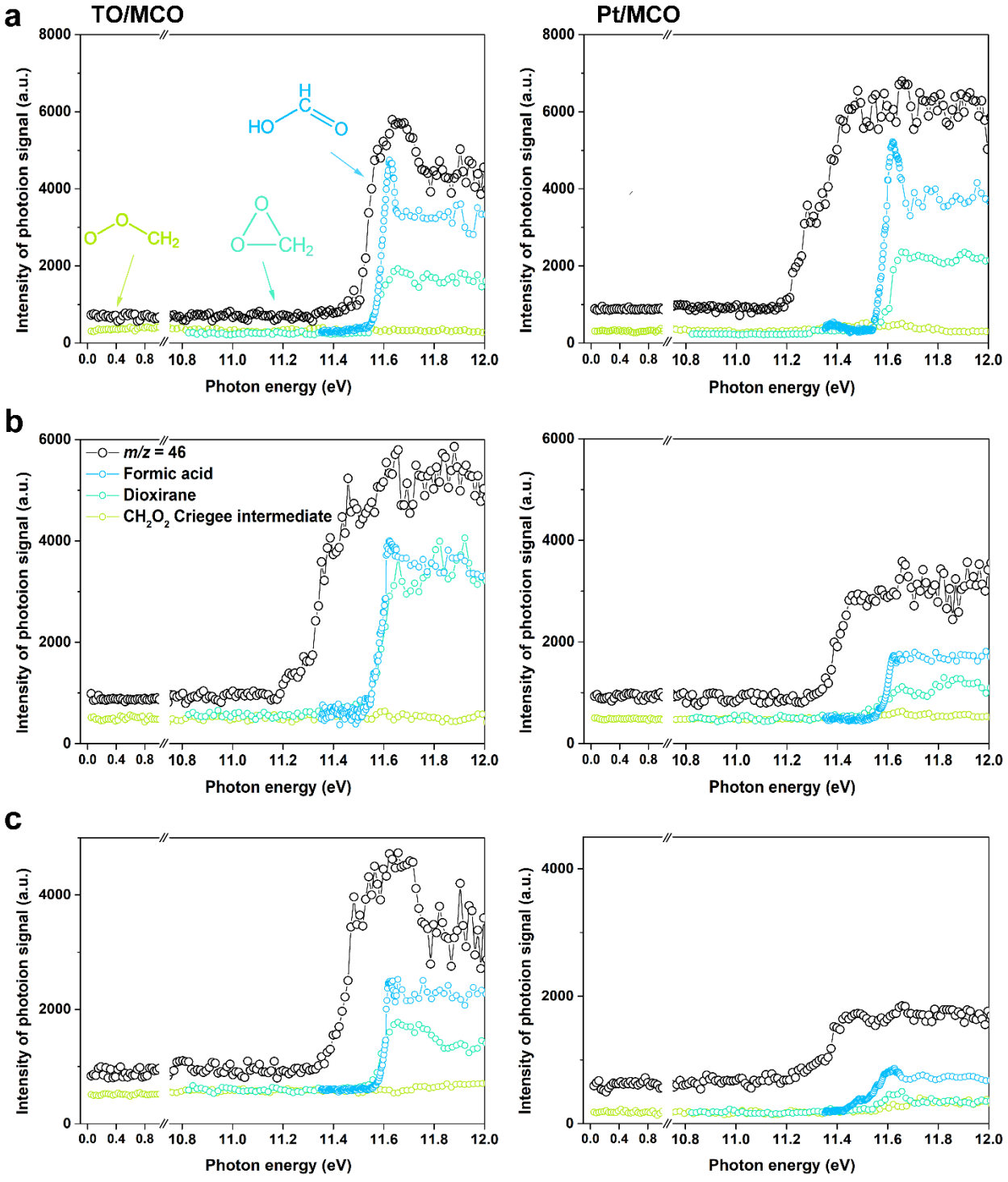

Figure 3. Determinations of the *m/z* = 46 species by the varying photoionization energies in the reaction of CH_2O with TO/MCO and Pt/MCO in different humid conditions at 72% (a and b), 50% (c and d), and 0.7% (e and f), respectively.

Changes in decay rates of CH_2OO in humid and dry feeds were examined under TO/MCO. The experimental lifetime of CH_2OO was sufficiently long to allow direct kinetic measurements in the continuous reaction. The reciprocal of the lifetime (τ) of CH_2OO is denoted as the decay rate in **Figure 4** and can arrive at constant within several milliseconds regardless of changes in reactant concentrations. Particularly, low relative humidity prohibits the adsorption and decomposition of CH_2O at ambient temperatures. **Figure 4a** shows that the decay rates of the signal integration of CH_2OO differed in humid and dry conditions. Approximately 6.6×10^3 s^{-1} of the decay rate of the CH_2OO group was attained in the humid feed, while the rate under TO/MCO was up to 4.0×10^3 s^{-1} in the dry feed. However, the rate for CH_2OO removal was found to be gradually slower than its formation due to the persistence of the CH_2O conversion, indicating that the CH_2OO lifetime was uncertain to experimentally estimate. As anticipated, the decay rate in dry air did not largely increase and the longest CH_2OO lifetime τ was estimated up to 0.5 ms in the dry air, which is four times faster than that estimated in the literature for approximately 2 ms in tropospheric Criegee reactions[2]. The decay rate of the three CH_2OO isomers after reaching an extremely short steady state was compared in the humid and dry feeds (**Figures 4b–c**). Their reaction kinetics are distinct but follow the same descending order: CH_2OO Criegee intermediate, formic acid, and dioxirane. By contrast, the very minor CH_2OO Criegee intermediate has the fast decay rate in humid (4.1×10^3 s^{-1}) and dry air (2.9×10^3 s^{-1}). The RCO of CH_2O, in coordination with the production, stabilization, and removal of CH_2OO, are preferable at higher humidity. In other words, the moisture-dependent decay of CH_2OO would restrict the RCO activity in practice.

In **Figure 4d,** a short C–O bond length (approximately 1.28 Å) and a long O–O bond (approximately 1.35 Å) of CH_2OO Criegee intermediate were observed[6, 43], as compared with

those of formic acid and dioxirane. The rapid kinetics of the Criegee intermediate are proven in trapping experiments with its scavenger NO_2 and SO_2 under tropospheric conditions[2, 5, 44]. Formaldehyde conversion to formic acid and dioxirane preferentially occurs through monodentate binding and bidentate coordination with metal sites of TO/MCO, respectively shown in **Figure 4e**. A peroxymethy bridging mode of –COO coordination with the active sites is thought to be more available for the dissociative adsorption of the weakened O–O than the strengthened C–O bond of CH_2OO Criegee intermediate.

Dioxirane has the longest lifespan and is formed possibly due to asymmetric isomerization of carboxylic bonds[2, 6, 43] as well. Moreover, its decay rate is slightly weaker than that of formic acid, suggesting the decomposition of dioxirane (C–O bond of approximately 1.40 Å) more refractory than formic acid (C=O bond of approximately 1.20 Å). If the O–H bond dissociation of hydroxyl and carboxylic bonds is sufficiently activated on metal sites of catalysts, then the remaining carboxylic groups would be bridged to epidioxyl groups of dioxirane under the electrophilic behavior of oxygen atoms[45]. Given that almost no reactions exist between epidioxyl and carboxylic groups at room temperatures, dioxirane is more inactive in the catalytic oxidation than two other intermediates. The formation and decay of CH_2OO Criegee are rather complex and remain unclear. CH_2OO Criegee is thought to possess some single bond characters[2, 6, 25, 43], which are assumed to a rapid dissociation of C–C and O–O bonds from the oxidation of unsaturated hydrocarbons. Furthermore, the linear relation between CH_2O disappearance and CH_2OO production is not fully understood[2, 3], in which small amounts of formaldehyde may be regenerated in reactions of O atom with CH_2OO Criegee intermediate. Consequently, preserving a large accumulation of CH_2OO on the surface of catalysts, such as dioxirane and formic acid which are more resistant to decomposition than CH_2O, is challenging to the complete catalytic

oxidation of CH_2O.

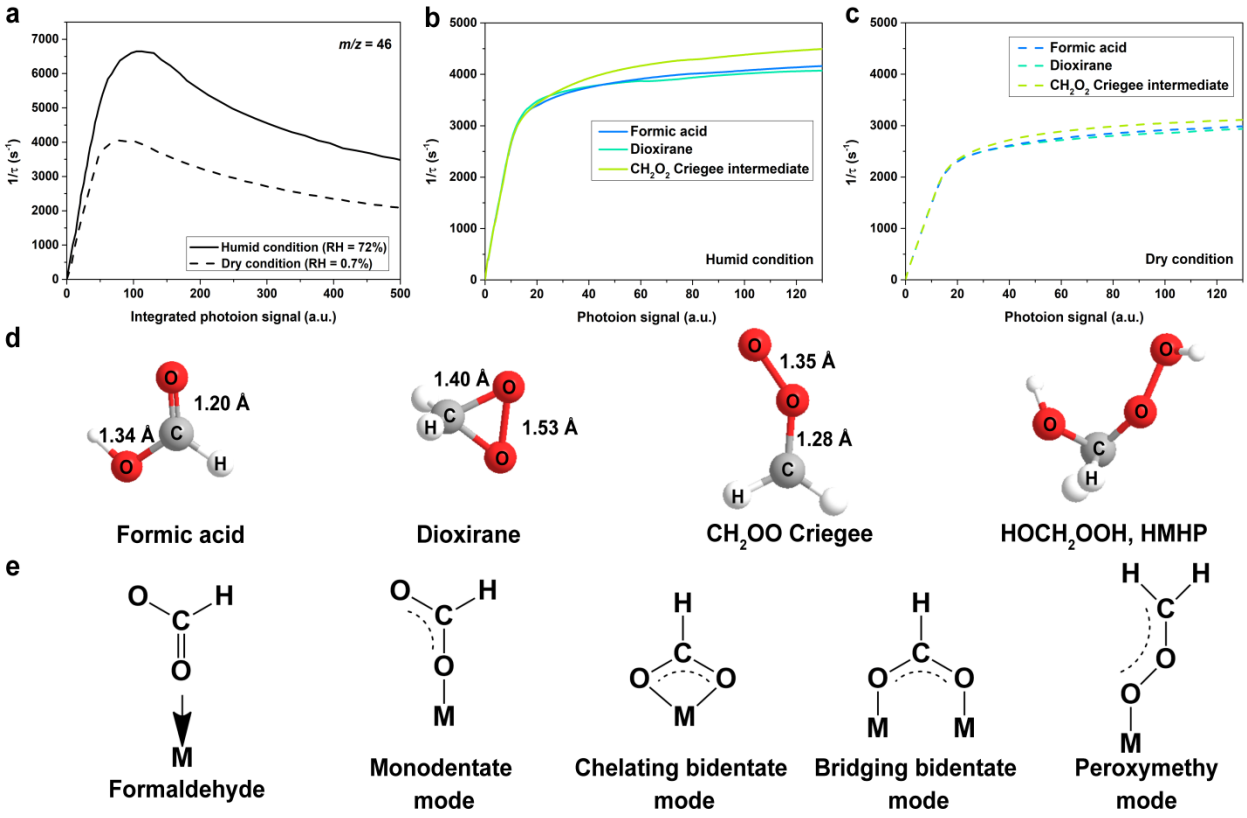

Figure 4. Decay rate (reciprocal of the lifetime τ) of integrated photoion signal of m/z = 46 species (a) and comparisons in the constant decay rate of photoion signals of three CH_2OO isomers during the CH_2O oxidation with TO/MCO in humid (b) and dry conditions (c). Geometries of three CH_2OO intermediates and very faint byproduct HMHP, indicating the preferential occurrence of CH_2OO reactions in moistures (d). Intermediates formed under the CH_2O oxidation with the surface metal site (M) of TO/MCO by the proposed bridging modes (e).

CH_2O Adsorption and Complete Oxidation Enhancement. RCO of CH_2O facilitates adsorption and favors high humidity. In this reaction, the initial physioadsorption relies on the improved specific surface areas and porosity followed by the chemisorption involving H bonding of methyl groups to interfacial water molecules[14, 21] and O atom bridging of carbonyl and carboxylic groups onto surface metal sites[20, 24, 45]. *In situ* C 1s XPS studies as a function of

reaction temperature were compared between the CH_2O-exposed TO/MCO and Pt/MCO (see **Figures 5a–b**). The broad photopeak at 288.5 eV was assigned to the presence of formaldehyde/mono(bi)-dentate formate species (C_F), and the photopeak at low BE (284.5 eV) was assigned to adventitious carbon (C_A)[17, 24]. As temperature increased from 25 °C to 45 °C, the ratios of C_F to C_A photopeak areas in Pt/MCO were all lower than those in TO/MCO. Better CH_2O/formate adsorption and oxidation were found at the surface of TO/MCO at ambient temperatures, consistent with the corresponding catalytic activities illustrated in **Figures 5c–d**. The adverse effects on the C_F intensity were apparent when temperature exceeded 45 °C. The decreases in C_F photopeak were larger in TO/MCO than in Pt/MCO at above 125 °C, indicating that the noble–metallic activity is preferentially at increased temperatures[46, 47]. C_A photopeak became precipitous at 125 °C–175 °C whereas weak CH_2O and formate signals were found in the C_F photopeak, indicative of CO and CO_2 yield in this temperature range[17]. The catalytic activity for the CH_2O removal was evaluated using the turnover frequencies (TOFs) per unit of surface area ($mol_{HCHO} \cdot s^{-1} \cdot m_{cat}^{-2}$), defined as the ratio of the reaction rate to the active-site density of catalysts. **Figure 5c** shows the variations in the CH_2O consumption rates with reaction temperatures over TO/MCO and Pt/MCO at different humid levels. The increased moistures in the feed positively affected CH_2O oxidation, but excessively high RH negatively influenced this reaction. The rate of TO/MCO decreased as temperature increased after the maximum of 6.6×10^{-8} $\mu mol_{HCHO} \cdot s^{-1} \cdot m_{cat}^{-2}$ was obtained at 35 °C. By contrast, the loading fabrication of Pt on the MCO surface resulted in the highest rate obtained at above 70 °C, matching with the *in situ* XPS results. Notably, when moisture decreased under the low-temperature range of 25 °C–45 °C, the consumption rates of TO/MCO were remediated because of its hydrophilic interface, approximately 30% higher than those of Pt/MCO. Hence, the TOFs of TO/MCO in the CH_2O

oxidation were much higher than those of Pt/MCO in the dry feed at low temperatures. The complete oxidation of by-product CO is reported to prefer under lower moistures[16]. In **Figure 5d**, the CH_2O conversion efficiencies to CO_2 were proportional to the TOFs under the identical test conditions and were reduced with the decreased moistures. The conversion rate largely decreases with an average of 22.6% for Pt/MCO in the dry air, whereas TO/MCO remained at 40.5% in the entire test. **Figure S10**

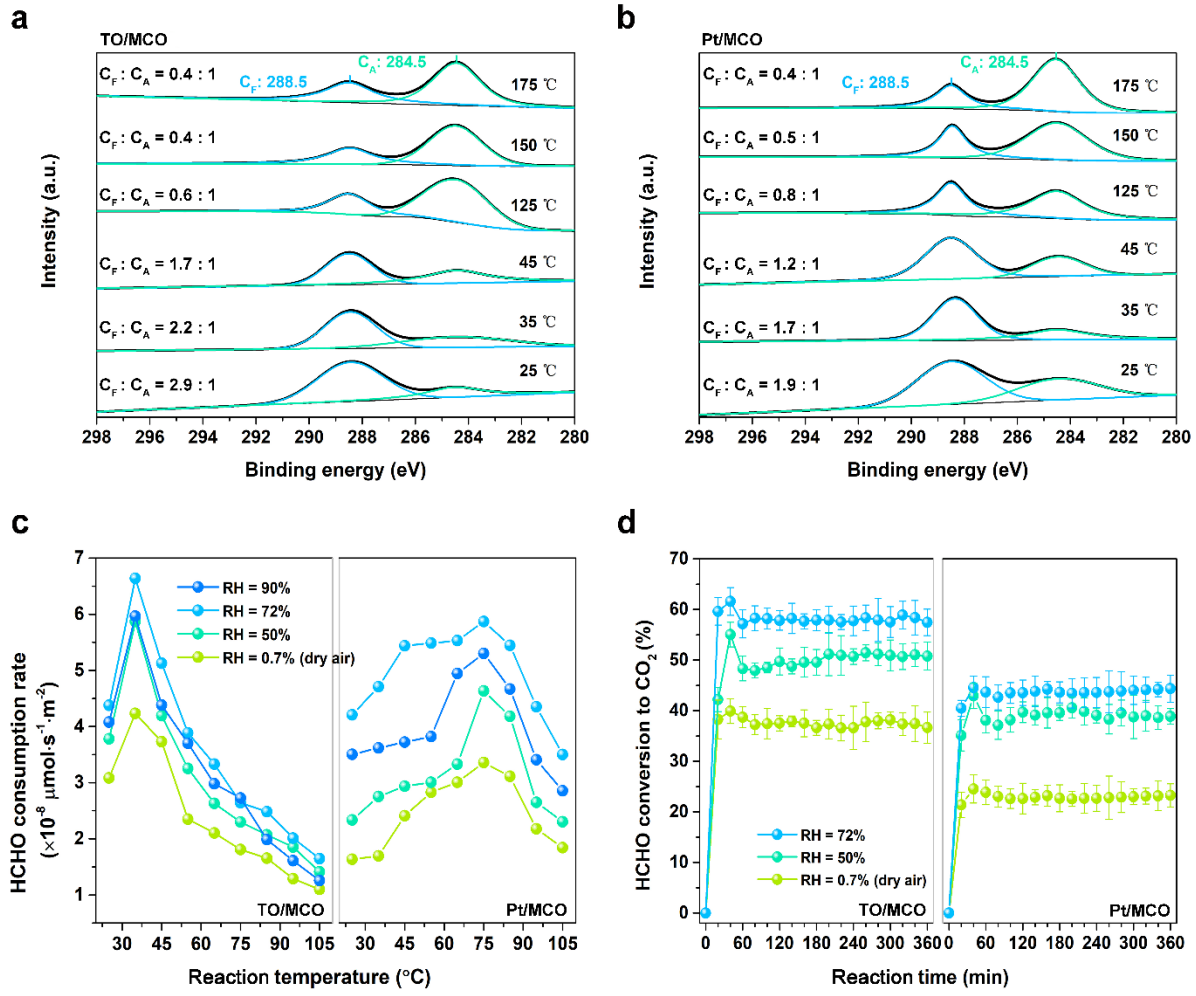

Figure 5. *In situ* C 1s XP spectra evolution of TO/MCO (a) and Pt/MCO (b) after CH_2O adsorption heating under Ar. Moisture-dependent CH_2O consumption rate as a function of reaction temperature (c). CH_2O conversion to CO_2 in different moistures during the isothermal

reaction at 35 °C (d).

Overall, the adsorption of CH_2O and CH_2OO intermediates was strongly initiated by the association of the H bond of alpha-methyl groups with the well-ordered interfacial water molecules in TO/MCO (see **Figures 1a–b**). In comparison with the subsequent decomposition of the ad-carboxylic (HO–C=O) groups, the H dissociation was likely stimulated at active sites on metal oxides (see **Figures 1c–d**). The C=O bond dissociation to C–O was triggered by the activation of reactive oxygen species at the identical active sites[20]. Consequently, exploring an ultrathin water/TiO_2 interface at catalysts is believed to enhance the complete adsorption and conversion of CH_2OO to CO_2 under unfavorable reaction moistures and temperatures.

Cytotoxicological Assessment of CH_2OO Intermediates. CH_2O is already recognized as a common environmental toxin even at low concentrations and has been long associated with the initiation and progression of diseases of the upper respiratory tract and several types of severe cancer[10, 26, 28]. To date, the toxicological potency of emissions from the CH_2OO intermediates has not yet been studied due to their uncertain speciation and milliseconds' lifetime. Because the cellular structure and organism function of yeast have many similarities with cells in plants and animals[48, 49], the cytotoxicity of the spent catalyst NPs (after the reaction was terminated at three given timeslots) exposed to yeast cells was evaluated as compared with the fresh NPs and formaldehyde did in **Figure 6**. As shown in **Figures 6a–c,** all cells stained by 4′,6-Diamidino-2-phenylindole (DAPI) were labeled with the green fluorophore and those with disrupted membrane stained by propidium iodide (PI) were labeled with the purple fluorophore in the FCSM images. After an initial 180 s reaction, the spent TO/MCO and Pt/MCO NPs in the FCSM images of the cell viability were observed to induce more apparent purple illuminations than those in MCO NPs, which were examined with the benign cell viability of their fresh NPs[20] (see

also **SI Figure S11**). Similarly, more purple fluorophores were highlighted under exposure to the spent catalysts after the prolonged reactions in 420 s. Hence, the cell membrane and cytoplasmic area are disrupted when the spent NPs are adhered to or transported into the yeast cells.

In **Figure 6d**, the fluorescence intensities of the cell-exposed spent NPs stained by PI were investigated to evaluate the cytotoxicity of the CH_2OO intermediates compared with those of cell exposure to a 0.017 mM CH_2O aqueous solution (approximately to 500 ppb of the initial gaseous CH_2O concentrations in the reaction). Interestedly, the PI fluorescence intensity of TO/MCO NPs inside the cell was more intense than that of Pt/MCO NPs, even more than CH_2O. Corresponding to large amounts of the generated CH_2OO intermediates at TO/MCO (see **Figure 3**), apart from formic acid, possible toxin species were assumed to the dioxirane and CH_2OO Criegee, resulting in more cell disruption and death.

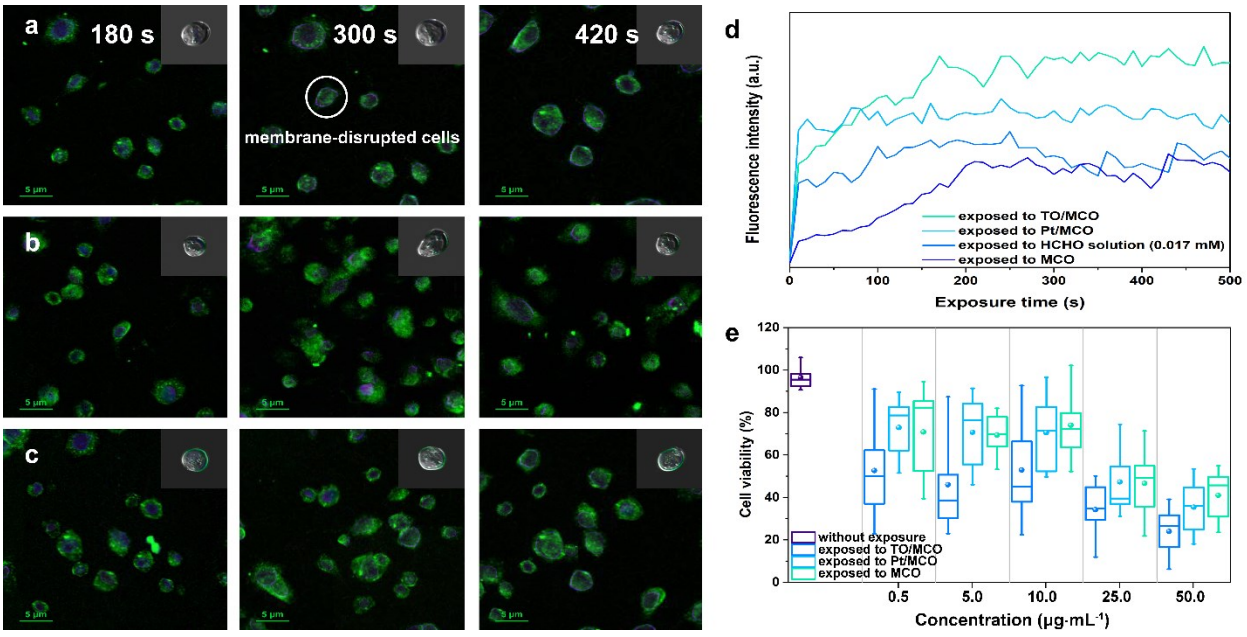

Figure 6. Time-lapse of confocal laser scanning microscope images of yeast cells exposed to spent TO/MCO (a), Pt/MCO (b), and MCO (c) NPs after the CH_2O oxidation was terminated at 180, 300, and 420 s, respectively. Disrupted cells stained by PI were labeled with a purple fluorophore, with the high-resolution 3D images shown in the inset. Fluorescence intensity of the

disrupted cells stained by PI after exposure to the NPs and 0.017 mM CH_2O solutions (d). Comparisons of cell viability after exposure to different concentrations of the three spent NPs using the CFUs counting method (e).

The number of CFUs of living yeast cells[50] was counted to double check the distinct cytotoxicity of the CH_2OO intermediates in **Figure 6e**. The yeast cells were exposed to the spent NPs with different concentrations of 0.5, 5, 10, 25, 50, and 100 $\mu g \cdot mL^{-1}$ dispersed in 5 mM aqueous NaCl solutions, respectively. The number of CFUs on the yeast-NP plate was compared with that of CFU on the control plate, which did not include NPs. The cell viabilities all weakened with the increase in concentrations of the NPs. Similarly, the spent Pt/MCO and MCO NPs stimulate more cell proliferation and less lethal than the spent TO/MCO NPs. An average of 50% of cell death occurred at the lowest 0.5 $\mu g \cdot mL^{-1}$ of NP concentrations and up to 80% of cell death was observed in the exposure to 50 $\mu g \cdot mL^{-1}$ TO/MCO NPs. Therefore, much larger amounts of CH_2O and CH_2OO intermediates can be adsorbed at the TO/MCO surface, thereby providing a basis for the complete conversion of CH_2O to CO_2 and suppressing toxic intermediate emissions to the ambient. This work also stimulates future study on the rational design and selectivity enhancement of reliable catalysts for practical applications under different ambient conditions.

ASSOCIATED CONTENT

Supporting Information. Preparations of the precursor MCO and TO/MCO catalysts; Fitted equation of SFG intensity; Schematic diagrams of SFG spectrometry and time-of-flight tunable synchrotron photoionization mass spectrometry; Voltammograms of TO/MCO and Pt/MCO in the SFG spectroelectrochemical measurements; Characterizations of XRD, TEM, BET, and XPS for as-prepared catalysts; Calibration of the time-of-flight photoion signal of m/z = 46 products;

Calibration of the photoionization spectra of CH_2OO by the varying photoionization energies; Catalytic activity of precursor MCO; Yeast cell viability observed by FCSM imaging after exposure to the fresh catalysts.

AUTHOR INFORMATION

Corresponding Authors

*Prof. Shun-cheng Lee (Email: ceslee@polyu.edu.hk)

*Dr. Wingkei Ho (Email: keithho@eduhk.hk)

Notes

The authors declare no competing interests.

Acknowledgements

This work was supported by the National Key Research and Development Program of China (2016YFA0203000), the Research Grants Council of Hong Kong Government (Project No. T24/504/17), the Research Grants Council of Hong Kong Government (PolyU152083/14E and PolyU152090/15E), and the Hong Kong RGC Collaborative Research Fund (C5022-14G).

REFERENCES

(1) Johnson, D.; Marston, G., The gas-phase ozonolysis of unsaturated volatile organic compounds in the troposphere. *Chem. Soc. Rev.* **2008,** *37*, (4), 699-716.

(2) Welz, O.; Savee, J. D.; Osborn, D. L.; Vasu, S. S.; Percival, C. J.; Shallcross, D. E.; Taatjes, C. A., Direct kinetic measurements of Criegee intermediate (CH_2OO) formed by reaction of CH_2I with O_2. *Science* **2012,** *335*, (6065), 204-207.

(3) Taatjes, C. A.; Welz, O.; Eskola, A. J.; Savee, J. D.; Scheer, A. M.; Shallcross, D. E.; Rotavera, B.; Lee, E. P.; Dyke, J. M.; Mok, D. K., Direct measurements of conformer-dependent reactivity of the Criegee intermediate CH_3CHOO. *Science* **2013,** *340*, (6129), 177-180.

(4) Welz, O.; Eskola, A. J.; Sheps, L.; Rotavera, B.; Savee, J. D.; Scheer, A. M.; Osborn, D. L.; Lowe, D.; Murray Booth, A.; Xiao, P., Rate coefficients of C1 and C2 Criegee intermediate reactions with formic and acetic acid near the collision limit: direct kinetics measurements and atmospheric implications. *Angew. Chem. Int. Ed.* **2014,** *53*, (18), 4547-4550.

(5) Chao, W.; Hsieh, J.-T.; Chang, C.-H., Direct kinetic measurement of the reaction of the simplest Criegee intermediate with water vapor. *Science* **2015,** *347*, (6223), 751-754.

(6) Su, Y.-T.; Huang, Y.-H.; Witek, H. A.; Lee, Y.-P., Infrared absorption spectrum of the simplest Criegee intermediate CH_2OO. *Science* **2013,** *340*, (6129), 174-176.

(7) Chen, L.; Huang, Y.; Xue, Y.; Cao, J.; Wang, W., Competition between HO_2 and H_2O_2 reactions with CH_2OO/anti-CH_3CHOO in the oligomer formation: a theoretical perspective. *J. Phys. Chem. A* **2017,** *121*, (37), 6981-6991.

(8) Su, Y.-T.; Lin, H.-Y.; Putikam, R.; Matsui, H.; Lin, M.; Lee, Y.-P., Extremely rapid self-reaction of the simplest Criegee intermediate CH_2OO and its implications in atmospheric

chemistry. *Nature Chem.* **2014,** *6*, (6), 477-483.

(9) Donahue, N. M.; Drozd, G. T.; Epstein, S. A.; Presto, A. A.; Kroll, J. H., Adventures in ozoneland: down the rabbit-hole. *Phys. Chem. Chem. Phys.* **2011,** *13*, (23), 10848-10857.

(10) Quiroz Torres, J.; Royer, S.; Bellat, J. P.; Giraudon, J. M.; Lamonier, J. F., Formaldehyde: catalytic oxidation as a promising soft way of elimination. *ChemSusChem* **2013,** *6*, (4), 578-592.

(11) Huang, H.; Xu, Y.; Feng, Q.; Leung, D. Y., Low temperature catalytic oxidation of volatile organic compounds: a review. *Catal. Sci. Technol.* **2015,** *5*, (5), 2649-2669.

(12) Nie, L.; Yu, J.; Jaroniec, M.; Tao, F. F., Room-temperature catalytic oxidation of formaldehyde on catalysts. *Catal. Sci. Technol.* **2016,** *6*, (11), 3649-3669.

(13) Xu, H.; Yan, N.; Qu, Z.; Liu, W.; Mei, J.; Huang, W.; Zhao, S., Gaseous heterogeneous catalytic reactions over Mn-based oxides for environmental applications: a critical review. *Environ. Sci. Technol.* **2017,** *51*, (16), 8879-8892.

(14) Wang, J.; Zhang, P.; Li, J.; Jiang, C.; Yunus, R.; Kim, J., Room-temperature oxidation of formaldehyde by layered manganese oxide: effect of water. *Environ. Sci. Technol.* **2015,** *49*, (20), 12372-12379.

(15) Kwon, D. W.; Seo, P. W.; Kim, G. J.; Hong, S. C., Characteristics of the HCHO oxidation reaction over Pt/TiO_2 catalysts at room temperature: the effect of relative humidity on catalytic activity. *Appl. Catal. B-Environ.* **2015,** *163*, 436-443.

(16) Wang, Y.; Zhu, X.; Crocker, M.; Chen, B.; Shi, C., A comparative study of the catalytic oxidation of HCHO and CO over $Mn_{0.75}Co_{2.25}O_4$ catalyst: the effect of moisture. *Appl. Catal. B-Environ.* **2014,** *160*, 542-551.

(17) Quiroz, J.; Giraudon, J. M.; Gervasini, A.; Dujardin, C.; Lancelot, C.; Trentesaux, M.;

505 Lamonier, J. F., Total oxidation of formaldehyde over MnO_x–CeO_2 catalysts: the effect of acid
506 treatment. *ACS Catal.* **2015,** *5*, 2260-2269.
507 (18) Tang, X.; Chen, J.; Huang, X.; Xu, Y.; Shen, W., Pt/MnO_x–CeO_2 catalysts for the complete
508 oxidation of formaldehyde at ambient temperature. *Appl. Catal. B-Environ.* **2008,** *81*, (1),
509 115-121.
510 (19) Han, X.; Li, C.; Liu, X.; Xia, Q.; Wang, Y., Selective oxidation of 5-hydroxymethylfurfural
511 to 2,5-furandicarboxylic acid over MnO_x–CeO_2 composite catalysts. *Green Chem.* **2017,** *19*,
512 (4), 996-1004.
513 (20) Li, H.; Huang, T.; Lu, Y.; Cui, L.; Wang, Z.; Zhang, C.; Lee, S.; Huang, Y.; Cao, J.; Ho, W.,
514 Unraveling the mechanisms of room-temperature catalytic degradation of indoor
515 formaldehyde and its biocompatibility on colloidal TiO_2-supported MnO_x–CeO_2. *Environ.*
516 *Sci-Nano* **2018,** *5*, (5), 1130-1139.
517 (21) Hussain, H.; Tocci, G.; Woolcot, T.; Torrelles, X.; Pang, C.; Humphrey, D.; Yim, C.; Grinter,
518 D.; Cabailh, G.; Bikondoa, O., Structure of a model TiO_2 photocatalytic interface. *Nature*
519 *Mater.* **2017,** *16*, (4), 461-466.
520 (22) Banerjee, S.; Dionysiou, D. D.; Pillai, S. C., Self-cleaning applications of TiO_2 by photo-
521 induced hydrophilicity and photocatalysis. *Appl. Catal. B-Environ.* **2015,** *176*, 396-428.
522 (23) Lu, Y., Self-hydrogenated shell promoting photocatalytic H_2 evolution on anatase TiO_2. *Nat.*
523 *Commun.* **2018,** *9*, (1), 2752-2760.
524 (24) Selvakumar, S.; Nuns, N.; Trentesaux, M.; Batra, V.; Giraudon, J.-M.; Lamonier, J.-F.,
525 Reaction of formaldehyde over birnessite catalyst: a combined XPS and TOF-SIMS study.
526 *Appl. Catal. B-Environ.* **2018,** *223*, 192-200.
527 (25) Hasson, A. S.; Chung, M. Y.; Kuwata, K. T.; Converse, A. D.; Krohn, D.; Paulson, S. E.,

528 Reaction of Criegee Intermediates with water vapor an additional source of OH radicals in
529 alkene ozonolysis? *J. Phys. Chem. A* **2003,** *107*, (32), 6176-6182.
530 (26) Salthammer, T.; Mentese, S.; Marutzky, R., Formaldehyde in the indoor environment. *Chem.*
531 *Rev.* **2010,** *110*, (4), 2536-2572.
532 (27) Burgos-Barragan, G.; Wit, N.; Meiser, J.; Dingler, F. A.; Pietzke, M.; Mulderrig, L.; Pontel,
533 L. B.; Rosado, I. V.; Brewer, T. F.; Cordell, R. L., Mammals divert endogenous genotoxic
534 formaldehyde into one-carbon metabolism. *Nature* **2017,** *548*, (7669), 549.
535 (28) Brewer, T. F.; Burgos-Barragan, G.; Wit, N.; Patel, K. J.; Chang, C. J., A 2-aza-cope
536 reactivity-based platform for ratiometric fluorescence imaging of formaldehyde in living cells.
537 *Chem. Sci.* **2017,** *8*, (5), 4073-4081.
538 (29) Noguchi, H.; Okada, T.; Uosaki, K., SFG study on potential-dependent structure of water at
539 Pt electrode/electrolyte solution interface. *Electrochim. Acta* **2008,** *53*, (23), 6841-6844.
540 (30) Ferreira de Morais, R.; Franco, A. A.; Sautet, P.; Loffreda, D., Interplay between reaction
541 mechanism and hydroxyl species for water formation on Pt(111). *ACS Catal.* **2015,** *5*, (2),
542 1068-1077.
543 (31) Noguchi, H.; Okada, T.; Uosaki, K., Molecular structure at electrode/electrolyte solution
544 interfaces related to electrocatalysis. *Faraday Discuss.* **2009,** *140*, 125-137.
545 (32) Zugic, B.; Wang, L.; Heine, C.; Zakharov, D. N.; Lechner, B. A.; Stach, E. A.; Biener, J.;
546 Salmeron, M.; Madix, R. J.; Friend, C. M., Dynamic restructuring drives catalytic activity on
547 nanoporous gold-silver alloy catalysts. *Nature Mater.* **2017,** *16*, (5), 558.
548 (33) Weng, X.; Sun, P.; Long, Y.; Meng, Q.; Wu, Z., Catalytic oxidation of chlorobenzene over
549 $Mn_xCe_{1-x}O_2$/HZSM-5 catalysts: a study with practical implications. *Environ. Sci. Technol.*
550 **2017,** *51*, (14), 8057-8066.

(34) Wang, J.; Wang, X.; Liu, X.; Zhu, T.; Guo, Y.; Qi, H., Catalytic oxidation of chlorinated benzenes over V_2O_5/TiO_2 catalysts: the effects of chlorine substituents. *Catal. Today* **2015,** *241*, 92-99.

(35) Van de Vyver, S.; Odermatt, C.; Romero, K.; Prasomsri, T.; Román-Leshkov, Y., Solid Lewis acids catalyze the carbon–carbon coupling between carbohydrates and formaldehyde. *ACS Catal.* **2015,** *5*, (2), 972-977.

(36) Yarulina, I.; Wispelaere, K. D.; Bailleul, S.; Goetze, J.; Radersma, M.; Abouhamad, E.; Vollmer, I.; Goesten, M.; Mezari, B.; Hensen, E. J. M., Structure-performance descriptors and the role of Lewis acidity in the methanol-to-propylene process. *Nature Chem.* **2018,** *10*, 804-812.

(37) Albonetti, S.; Blasioli, S.; Bonelli, R.; Mengou, J. E.; Scirè, S.; Trifirò, F., The role of acidity in the decomposition of 1,2-dichlorobenzene over TiO_2-based V_2O_5/WO_3 catalysts. *Appl. Catal. A-Gen.* **2008,** *341*, (1-2), 18-25.

(38) Feng, X.; Sayle, D. C.; Wang, Z. L.; Paras, M. S.; Santora, B.; Sutorik, A. C.; Sayle, T. X.; Yang, Y.; Ding, Y.; Wang, X., Converting ceria polyhedral nanoparticles into single-crystal nanospheres. *Science* **2006,** *312*, (5779), 1504-1508.

(39) Zhang, C.; Michaelides, A.; King, D. A.; Jenkins, S. J., Anchoring sites for initial Au nucleation on CeO_2(111): O vacancy versus Ce vacancy. *J. Phys. Chem. C* **2009,** *113*, (16), 6411-6417.

(40) Yan, Z. X., Zhihua; Yu, Jiaguo; Jaroniec, Mietek, Highly active mesoporous ferrihydrite supported catalyst for formaldehyde removal at room temperature. *Environ. Sci. Technol.* **2015,** *49*, (11), 6637-6644.

(41) Duan, B.; Yang, J.; Salvador, J. R.; He, Y.; Zhao, B.; Wang, S.; Wei, P.; Ohuchi, F. S.;

574 Zhang, W.; Hermann, R. P., Electronegative guests in $CoSb_3$. *Energ. Environ. Sci.* **2016,** *9*,
575 (6), 2090-2098.
576 (42) Lu, Y.; Huang, Y.; Zhang, Y.; Cao, J.-j.; Li, H.; Bian, C.; Lee, S. C., Oxygen vacancy
577 engineering of $Bi_2O_3/Bi_2O_2CO_3$ heterojunctions: Implications of the interfacial charge
578 transfer, NO adsorption and removal. *Appl. Catal. B-Environ.* **2018,** *231*, 357-367.
579 (43) Nguyen, M. T.; Nguyen, T. L.; Ngan, V. T.; Nguyen, H. M. T., Heats of formation of the
580 Criegee formaldehyde oxide and dioxirane. *Chem. Phys. Lett.* **2007,** *448*, (4), 183-188.
581 (44) Vereecken, L.; Harder, H.; Novelli, A., The reaction of Criegee intermediates with NO, RO_2,
582 and SO_2, and their fate in the atmosphere. *Phys. Chem. Chem. Phys.* **2012,** *14*, (42), 14682-
583 14695.
584 (45) Jia, X.; Ma, J.; Xia, F.; Xu, Y.; Gao, J.; Xu, J., Carboxylic acid-modified metal oxide
585 catalyst for selectivity-tunable aerobic ammoxidation. *Nat. Commun.* **2018,** *9*, (1), 933-939.
586 (46) Zhang, C.; Li, Y.; Wang, Y.; He, H., Sodium-promoted Pd/TiO_2 for catalytic oxidation of
587 formaldehyde at ambient temperature. *Environ. Sci. Technol.* **2014,** *48*, (10), 5816-5822.
588 (47) Chen, B.-b.; Zhu, X.-b.; Crocker, M.; Wang, Y.; Shi, C., FeO_x-supported gold catalysts for
589 catalytic removal of formaldehyde at room temperature. *Appl. Catal. B-Environ.* **2014,** *154*,
590 73-81.
591 (48) Nomura, T.; Miyazaki, J.; Miyamoto, A.; Kuriyama, Y.; Tokumoto, H.; Konishi, Y.,
592 Exposure of the yeast saccharomyces cerevisiae to functionalized polystyrene latex
593 nanoparticles: influence of surface charge on toxicity. *Environ. Sci. Technol.* **2013,** *47*, (7),
594 3417-3423.
595 (49) Eigenheer, R.; Castellanos, E. R.; Nakamoto, M. Y.; Gerner, K. T.; Lampe, A. M.; Wheeler,
596 K. E., Silver nanoparticle protein corona composition compared across engineered particle

properties and environmentally relevant reaction conditions. *Environ. Sci-Nano* **2014,** *1*, (3), 238-247.

(50) Huang, Y.; Liang, Y.; Rao, Y.; Zhu, D.; Cao, J.-j.; Shen, Z.; Ho, W.; Lee, S. C., Environment-friendly carbon quantum dots/$ZnFe_2O_4$ photocatalysts: characterization, biocompatibility, and mechanisms for NO removal. *Environ. Sci. Technol.* **2017,** *51*, (5), 2924-2933.

603

TOC Art

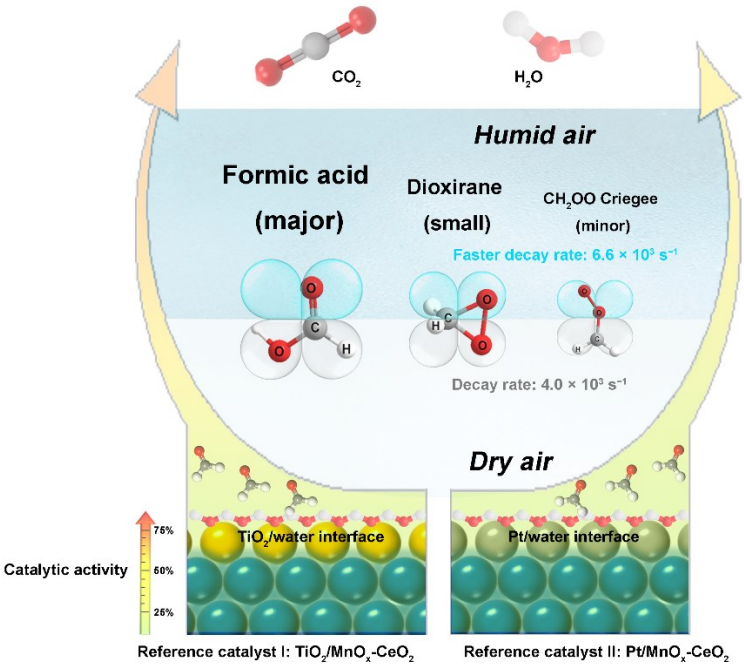

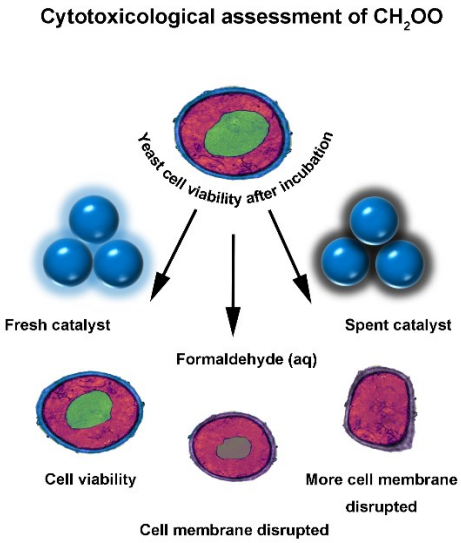

604